


Cite this: *RSC Adv.*, 2023, 13, 34703

Interpretation of dielectric behavior and polaron hopping in lead-free antimony-based double perovskite

Mohamed Ben Bechir ^{*a} and Faisal Alresheedi^b

Lately, double perovskite materials have become well-known in the commercialization area owing to their potential use in optoelectronic applications. Here, double perovskite $\text{Cs}_2\text{AgSbCl}_6$ single crystals (SCs) with cubic crystal structure and $Fm\bar{3}m$ space group were successfully synthesized via the slow cooling technique. This paper investigates the dielectric relaxation and charge transfer mechanism within $\text{Cs}_2\text{AgSbCl}_6$ using electrochemical impedance spectroscopy (EIS) in the 273–393 K temperature range under light. The dielectric response in $\text{Cs}_2\text{AgSbCl}_6$ has been explained by the space charge polarization and the ionic motion. The $\epsilon''(\omega)$ study at different temperatures shows a remarkable frequency transition at which $d\epsilon''/dT$ changes from a positive to a negative coefficient. Based on Stevels approach, the density of traps diminishes with the temperature increase, which improved conduction. However, this approach proves the polaronic conduction in $\text{Cs}_2\text{AgSbCl}_6$. 0.42 and 0.21 eV are the binding (E_p) and polaron hopping (W_H) energy values, respectively. Contrary to free-charge carrier motion, polaron hopping was proposed as the principal conduction process since the ambient-temperature thermal energy was lower than E_p . Moreover, the analysis of $M''(\omega)$ and $-Z''(\omega)$ as a function of temperature shows the thermally-activated relaxation from the non-Debye to Debye type model in $\text{Cs}_2\text{AgSbCl}_6$. This scientific research offers an essential understanding of the dielectric relaxation behavior, which is required for improving dielectric switches. Also, this paper provides a deep insight into the conduction mechanism within double perovskite materials.

Received 28th August 2023
Accepted 16th November 2023
DOI: 10.1039/d3ra05857c
rsc.li/rsc-advances

1. Introduction

Recently, lead (Pb)-based halide perovskites, which have shown power conversion efficiencies above 25.5%, have drawn researchers' attention as potential materials in place of silicon solar cells.^{1–3} These semiconducting materials, which can be prepared through inexpensive precursors, show interesting optoelectronic proprieties as high absorption coefficients, tunable band gap, and excellent charge carrier mobility marked by a good lifetime.^{4–6} However, despite all these performances, researchers are looking for alternatives to lead (Pb)-based halide perovskites due to their chemical instabilities and lead toxicity.⁷

In this context, a promising approach is the heterovalent replacement of the lead (Pb) position in the crystal structure by a pair of monovalent and trivalent metal ions, forming the well-known metal-halide lead-free halide double perovskites with $\text{A}_2\text{MM}'\text{X}_6$ ($\text{A} = \text{Rb}^+$, Cs^+ , etc.; $\text{M} = \text{Ag}^+$, K^+ , Li^+ ; $\text{M}' = \text{Sb}^{3+}$, In^{3+} or Bi^{3+} and $\text{X} = \text{I}^-$, Br^- or Cl^-).⁸ In the context of ferroelectrics, the

double perovskite materials have analyzed for the first time in the 1970s.⁹ Until now, a large number of double perovskite compounds, which have good octahedral and Goldschmidt tolerance factors, have been predicted to be chemically stable.^{10,11} Thus, the thermodynamic stability with the structural and functional variety noted in this family, shows that the metal-halide lead-free halide double perovskites are promised candidates for optoelectronic applications.^{11–13} The Cs_2AgMX_6 compound, with M representing Bi, Sb, or In, exhibits a highly encouraging structure for lead-free halide perovskites due to the interconnection of metal halide octahedra throughout a three-dimensional framework.¹⁴ This extensive three-dimensional interconnection possibly underlies the notable performance in photovoltaic devices crafted from these substances. Notably, these devices have demonstrated remarkably high power conversion efficiencies, surpassing those reported for other lead-free halide materials, despite having band gaps of an indirect nature.^{15,16} In recent studies, numerous scientific teams have presented methods for creating nanocrystals of $\text{Cs}_2\text{AgBiX}_6$ (X referring to Br or Cl).^{17–20} Discrepancies have emerged in the observed optical spectra when comparing nanocrystal data to measurements obtained from bulk materials. Notably, observations of a distinct peak at 430 nm in $\text{Cs}_2\text{AgBiBr}_6$ have raised questions, hinting at the possibility of substantial quantum

^aLaboratory of Spectroscopic and Optical Characterization of Materials (LaSCOM), Faculty of Science, University of Sfax, BP1171, 3000 Sfax, Tunisia. E-mail: mohamedbenbechir@hotmail.com

^bDepartment of Physics, College of Science, Qassim University, Buraidah 51452, Saudi Arabia



confinement within these specific systems. Earlier investigations suggested that the discrepancies observed could be attributed to differences in measurement techniques (specifically, transmission *versus* reflection) and variations in sample concentration rather than stemming from the inherent optical response.^{18,21} Further reinforcement for this hypothesis was obtained through the examination of thin film transmission in single-crystalline $\text{Cs}_2\text{AgBiBr}_6$,²² demonstrating remarkably similar optical characteristics to the nanocrystal solutions.

Despite the A_2MSbX_6 compounds presenting the advantage of lower bandgap since they have a reduced conduction band minimum, these compounds are the less studied double perovskites.^{12,13} However, the synthesis of $\text{Cs}_2\text{AgSbCl}_6$ perovskite was carried out using a limited number of different techniques. Recently a scientific team effectively produced polycrystalline $\text{Cs}_2\text{AgSb}_{1-x}\text{In}_x\text{Cl}_6$ samples by utilizing solid-state methods. This involved combining specific amounts of CsCl , AgCl , and SbCl_3 (or InCl_3) in evacuated quartz ampules, followed by heating the mixture to 400 °C.²³ Subsequently, a separate group of researchers prepared $\text{Cs}_2\text{AgSbCl}_6$ microcrystals using the hydrothermal technique within a stainless-steel Parr autoclave. The resultant crystals displayed a tetracahedral crystallization pattern, forming a truncated octahedral structure.²⁴ Lately, the hot injection method was employed to create colloidal nanocrystals (NCs) of $\text{Cs}_2\text{AgSb}_{1-x}\text{Bi}_x\text{Cl}_6$ alloys, as detailed in the recent study.²⁵ This process yielded NCs exhibiting a cubic morphology. Nevertheless, detailed studies on dielectric relaxation and conduction mechanism within the A_2MSbX_6 double perovskites are not yet noticed. Thus, for better enhancement of these double perovskites in dielectric and optoelectronic applications, a comprehensive understanding of the fundamental physical processes in A_2MSbX_6 is needed.

In this work, the elaboration, as well as structural and optical studies of $\text{Cs}_2\text{AgSbCl}_6$, are represented. This paper offers a comprehensive knowledge of dielectric relaxation and conduction mechanisms in $\text{Cs}_2\text{AgSbCl}_6$. EIS is a powerful technique for investigating dielectric characteristics. This work contains a detailed frequency and temperature-dependent study of dielectric relaxation within $\text{Cs}_2\text{AgSbCl}_6$. It was found that the dielectric constant falls at a transition frequency, which increases with the temperature. Stevels model proves that polaron hopping is the principal conduction mechanism in $\text{Cs}_2\text{AgSbCl}_6$, and indicates the decreasing of confined charge density when the temperature increases and then conduction improves. The combined modulus and impedance analyses show the thermally-activated relaxation from the non-Debye to Debye type model in $\text{Cs}_2\text{AgSbCl}_6$.

Our paper, which gives thorough comprehension and new ideas about polaron hopping and dielectric relaxation within $\text{Cs}_2\text{AgSbCl}_6$ can be valuable to different lead-free halide double perovskite materials.

2. Methods

2.1 Materials

Cesium chloride (Sigma-Aldrich, $\geq 98.0\%$), silver chloride (Sigma-Aldrich, 99.99%), and antimony(III) chloride (Sigma-

Aldrich, $\geq 99.95\%$) were used as obtained without further purification. HCl was prepared from Synth, 37% wt in water.

2.2 Synthesis

Black pyramid-like $\text{Cs}_2\text{AgSbCl}_6$ SCs were synthesized by the solvothermal procedure (Fig. 1a), which is ensured by the slow cooling method. The precursor CsCl (0.95097 g, 0.0056485 mol), AgCl (0.40477 g, 0.0028242 mol), and SbCl_3 (0.64426 g, 0.0028242 mol) salts were dissolved in distilled water according to the following equation:



The solution obtained was meticulously transferred into a 15 mL Teflon-lined SS autoclave and then placed in an oven set at 150 °C. Next, the precursor solution was cooled from 150 °C to room temperature at a rate of 0.25 °C h⁻¹ instead of the natural cooling method. Later achieving ambient temperature, the precursor solution was left for some days (at room temperature). In the end, the $\text{Cs}_2\text{AgSbCl}_6$ SCs were later grown by slow solvent evaporation. Based on previous work on $\text{Cs}_2\text{-CuSbCl}_6$ SCs,²⁶ this method of synthesis can lead to $\text{Cs}_2\text{AgSbCl}_6$ nanoparticles.

2.3 Characterizations

The powder X-ray diffraction (PXRD) analysis was performed at room temperature by the Rigaku MiniFlex 600 benchtop diffractometer using $\text{Cu(K}\alpha\text{)}$ line radiation ($\lambda = 1.54 \text{ \AA}$).

HAADF-STEM pictures and Energy Dispersive X-ray Spectroscopy (EDS) data were collected with a Cs-corrected JEOL JEM-2100 F microscope set to 200 kV. A JEOL Silicon Drift Detector (DrySD60GV) with a sensor size of 60 mm² was used for EDS mapping, spanning an estimated solid angle of 0.5 steradians.

The thermogravimetric (TG) study was performed on a PerkinElmer Pyris 6 in the temperature range of 300–1300 K with a heating rate of 5 °C min⁻¹.

The diffuse reflectance spectrum was registered at room temperature *via* a PerkinElmer Lambda 950 UV-Vis spectrophotometer.

At room temperature, the photoluminescence (PL) spectra were obtained using a HORIBA LabRAM (HR800) apparatus equipped with a 325 nm laser. The TRPL (Time-Resolved Photoluminescence) analysis was conducted using a Time-Correlated Single Photon Counting (TCSPC) system (Horiba Jobin Yvon Inc). The TCSPC measurements were performed utilizing a pulsed-laser source operating at a wavelength of 325 nm, with a repetition rate of 100 kHz, fluence approximately at 4 nJ cm⁻², and a pulse width of 70 ps. In this study, $\text{Cs}_2\text{-AgSbCl}_6$ SCs were excited using a 325 nm wavelength *via* a xenon lamp source under room temperature. The Ludox suspension was employed as the instrument's response function to deconvolute the spectral values.

Raman measurements were taken with the Horiba LabRAM HR Evolution Raman Spectrometer to investigate the $\text{Cs}_2\text{-AgSbCl}_6$ SCs.



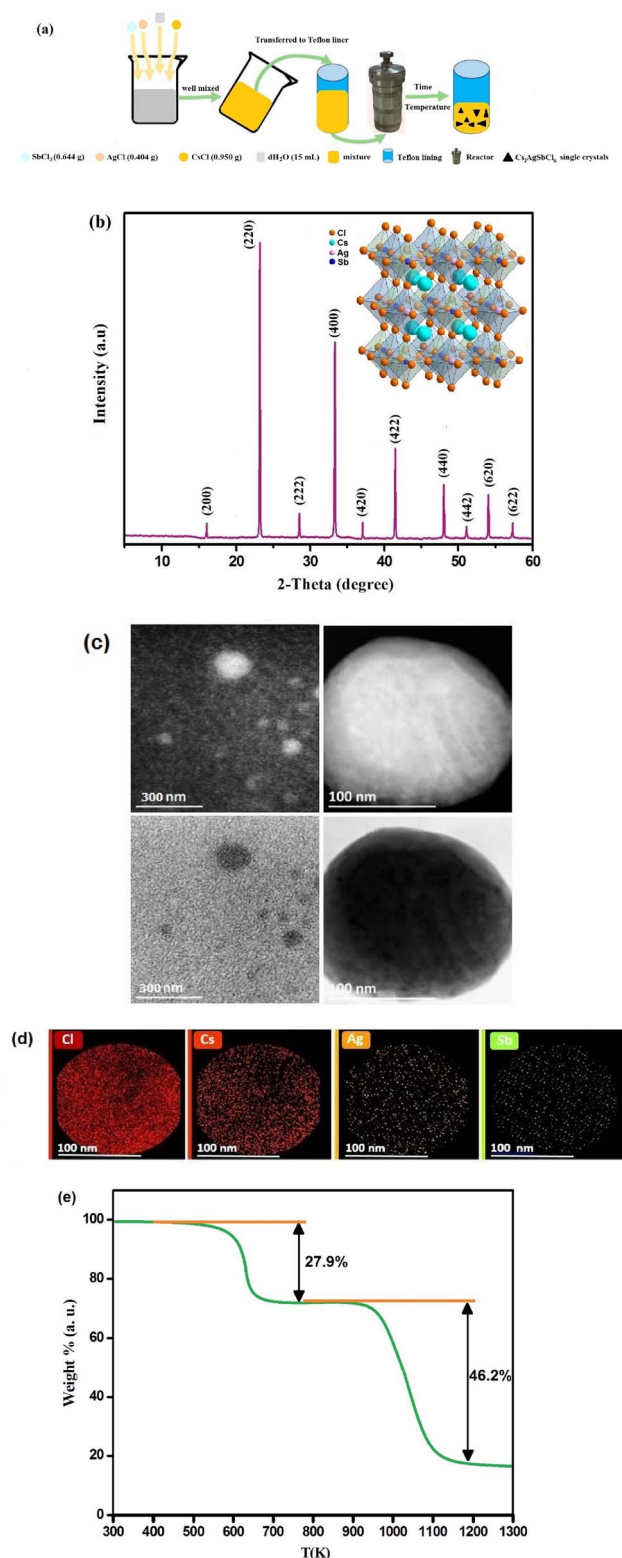


Fig. 1 (a) Schematic picture of the solvothermal method to obtain $\text{Cs}_2\text{AgSbCl}_6$ single crystals. (b) Powder X-ray diffractogram of $\text{Cs}_2\text{AgSbCl}_6$ at room temperature in the 2θ range 5–60°. The inset presents the packing diagram for $\text{Cs}_2\text{AgSbCl}_6$. (c) STEM-HAADF image of $\text{Cs}_2\text{AgSbCl}_6$. (d) EDS mapping of Cs, Ag, Sb and Cl in different colors. (e) TG data of $\text{Cs}_2\text{AgSbCl}_6$ in the temperature range of 300–1300 K.

To evaluate the complex impedance, a small portion of $\text{Cs}_2\text{AgSbCl}_6$ SCs underwent mechanical grinding in an agate mortar with a pestle to produce fine powders. A pellet of $\text{Cs}_2\text{AgSbCl}_6$, measuring 0.92 mm in thickness and with a relative density of 95.17%, was prepared at room temperature by subjecting it to a 50 Torr pressure using an 8 mm diameter hydraulic press. The pellet obtained was positioned between a pair of copper electrodes, with a layer of silver paint applied to ensure effective electrical contact between the sample and the electrodes. The impedance measurements under light and at different temperatures (273–393 K) were done using the Zahner electrochemical workstation in the frequency range of $10\text{--}10^6$ Hz.

Ultrafast transient absorption (TA) observations were performed using the Helios pump-probe ultrafast spectroscopy equipment. This cutting-edge setup comprised a laser oscillator (Coherent Micra) functioning on Ti: sapphire principles, an amplifier (Coherent Legend), and an optical parametric amplifier (OPA) (TOPAS) furnished with a crystal of Barium Borate (BBO). Transient absorption (TA) measurements on an ultrafast timescale were executed using this arrangement. An amplified laser pulse is produced by the amplifier, displaying a Gaussian profile and lasting around 35 fs. This pulse is centered at 700 nm and holds an average power of 3.5 W, operating at a frequency of 1 kHz. The divided amplified laser beam undergoes bifurcation, with 70% being steered towards the optical parametric amplifier (OPA), and the residual 30% being routed towards the spectrometer. To facilitate a time delay, a delay stage encompassing a span from 0 to 8 ns is incorporated. This temporal offset allows the allocated 30% portion of the beam to function as the probe beam for purposes of spectroscopic examination. The process of generating a white-light continuum (WLC) for the probe beam, spanning from 375 nm to 750 nm, involves guiding the bifurcated beam through a sapphire plate. Extracting a pump beam at around 350 nm wavelength was achieved by tapping into the exceptionally consistent output of the optical parametric amplifier (OPA). This particular pump beam carried a fluence measuring 0.5 mW. With meticulous attention, both the pump and probe beams were precisely concentrated onto the sample to guarantee impeccable spatial congruity. The manipulation of data and its subsequent fitting were accomplished through the utilization of the surface Xplorer software. To establish the spectral resolution, an in-house calibrated ocean optics spectrometer was employed alongside the ZnTPP dye for calibration purposes.

3. Results and discussion

The room temperature PXRD pattern of $\text{Cs}_2\text{AgSbCl}_6$ is presented in Fig. 1b. With the Celref 3 software's help,²⁷ it was found that $\text{Cs}_2\text{AgSbCl}_6$ crystallizes at room temperature in the cubic symmetry with $Fm\bar{3}m$ space group and lattice parameters $a = b = c = 10.3954$ Å. This result is in good accord with the literature.²⁸ The crystal structure of $\text{Cs}_2\text{AgSbCl}_6$, which is shown in the inset of Fig. 1b, contains corner-shared $[\text{AgCl}_6]^{5-}$ and $[\text{SbCl}_6]^{3-}$ octahedra arranged alternately periodically. All the



cesium atoms (Cs) are positioned in the cubic octahedral cavity, thus constituting a double perovskite structure.²⁸

Morphological attributes and particle shape of Cs₂AgSbCl₆ SCs were scrutinized through the utilization of transmission electron microscopy (TEM) imaging. An illustrative depiction of the sample is presented in Fig. 1c. The assessment divulged that a significant proportion of particles displayed a diminutive spherical configuration. In particular, the exploration of an individual spherical particle measuring around 200 nm in size is depicted in Fig. 1c. To verify the existence of chemical constituents within the synthesized Cs₂AgSbCl₆, a STEM-EDS analysis was carried out, as depicted in Fig. 1d. The analysis through EDS mapping unveiled the presence of cesium (Cs), silver (Ag), antimony (Sb), and chloride (Cl). This outcome serves as evidence that no elements underwent depletion throughout the entirety of the synthesis process. From these findings, it is implied that the prepared Cs₂AgSbCl₆ is of complete purity, as detailed in Table 1. The chemical elements existing within Cs₂AgSbCl₆ can be theoretically computed as follows:

$$\begin{aligned}
 2\text{Cs} + \text{Ag} + \text{Sb} + 6\text{Cl} &= 100\% \\
 \rightarrow \text{Cs} &= 20\% \approx 20.5\% \\
 \rightarrow \text{Ag} &= 10\% \approx 10.1\% \\
 \rightarrow \text{Sb} &= 10\% \approx 9.8\% \\
 \rightarrow \text{Cl} &= 60\% \approx 59.6\%
 \end{aligned}
 \quad (1)$$

The TG study of the Cs₂AgSbCl₆ compound is presented in Fig. 1e. The decomposition of the prepared perovskite appears in two steps around 600 and 987 K.

The absorption spectrum of Cs₂AgSbCl₆ from 250 to 450 nm at room temperature is shown in Fig. 2a. A Tauc study on the absorption spectrum of Cs₂AgSbCl₆ powder (inset of Fig. 2) suggests an indirect bandgap (E_g) of 2.52 eV, which is in accord with the literature.¹¹

The PL spectrum displays a peak situated at 396 nm, as illustrated in Fig. 2b. This aligns harmoniously with earlier investigations.^{29,30} Furthermore, an assessment of time-resolved photoluminescence (TRPL) was carried out on Cs₂AgSbCl₆ SC at room temperature, as shown in Fig. 2c. The outcomes unveiled an appreciably protracted carrier lifetime of 8.21 ns, surpassing the value of 6.57 ns found previously.³¹ This elongated carrier lifetime stands as a testament to the enhanced excellence and diminished imperfections in the Cs₂AgSbCl₆ SC.

The Raman spectra of the Cs₂AgSbCl₆ SC at room temperature is shown in Fig. 2d. The literature has been used to provide a full attribution.^{32–34} The vibrational patterns within Cs₂AgSbCl₆ SC predominantly manifest in the lower-wavenumber

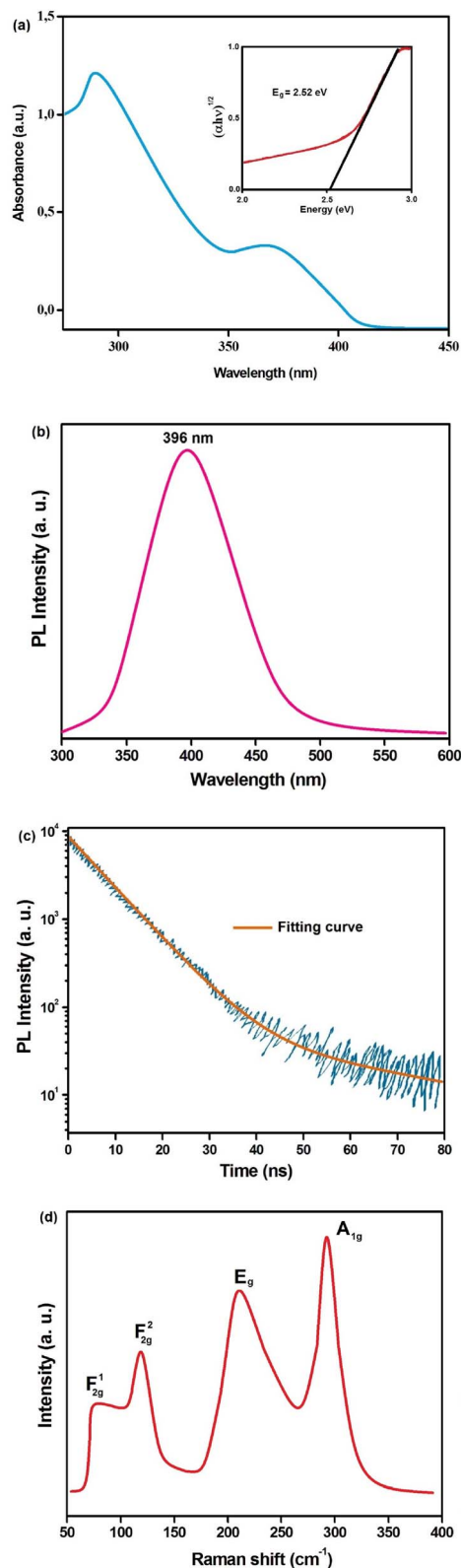


Fig. 2 (a) Absorption spectrum of Cs₂AgSbCl₆. The inset shows the Tauc plot. (b) Photoluminescence spectrum of Cs₂AgSbCl₆. (c) Time-resolved PL spectrum of Cs₂AgSbCl₆ at room temperature. (d) Raman spectrum of Cs₂AgSbCl₆SC obtained at room temperature.

Table 1 Composition analysis: chemical elements proportions in Cs₂AgSbCl₆ SC

Chemical element	% atomic
Caesium (Cs)	20.5
Silver (Ag)	10.1
Antimony (Sb)	9.8
Chloride (Cl)	59.6



domain, extending up to 310 cm^{-1} . This phenomenon arises from the inclusion of substantial elements such as Ag and Sb within their composition. While the octahedral structures of $[\text{SbCl}_6]^{5-}$ and $[\text{AgCl}_6]^{5-}$ exhibit impeccable O_h symmetry, variations in the bond lengths of Ag-Cl and Sb-Cl contribute to distinct sizes of their respective octahedra. Due to the slightly greater Ag-Cl bond lengths in comparison to the Sb-Cl bond lengths, the $[\text{SbCl}_6]^{5-}$ octahedron exhibits a more robust bond.⁷ Consequently, it is foreseeable that the vibrational reaction within these SCs will be predominantly influenced by the $[\text{SbCl}_6]^{5-}$ octahedron in contrast to the $[\text{AgCl}_6]^{5-}$ octahedron. The lower-frequency resonance at 73 cm^{-1} corresponds to the translational mode, with the 122 cm^{-1} registering as an overtone of this mode. Meanwhile, the higher-frequency resonances at 209 cm^{-1} and 294 cm^{-1} can be attributed to the E_g (stretching asymmetric) and A_{1g} (stretching symmetric) modes of the octahedron, respectively. The allocations to these diverse modes are additionally validated by adhering to the subsequent over-arching relationship:

$$U_{A_{1g}}^2 = U_{E_g}^2 + \frac{3}{2}U_{T_{2g}}^2 \quad (2)$$

Examination of Table 2 showcases a satisfactory alignment between the acquired experimental frequencies and the documented outcomes from DFT analysis.

The impedance analysis has been carried out under illumination in the 273–393 K temperature range to understand the conduction mechanism and dielectric relaxation behavior within $\text{Cs}_2\text{AgSbCl}_6$. Fig. 3a shows the $Z'(\omega)$ plots in different temperatures. It is noted that, at low frequencies, the resistance (Z') reduces when both temperature and frequency increase, which suggests the NTCR (negative temperature coefficient of the resistance) comportment in $\text{Cs}_2\text{AgSbCl}_6$.³⁵ This increasing conductance with the temperature can be explained by the augmentation of charge carrier mobility besides the decrease in confined charge density within $\text{Cs}_2\text{AgSbCl}_6$.³⁶ As shown in the inset of Fig. 3a, below a particular frequency we note a negative coefficient (NC) for dZ'/dT , which becomes a positive coefficient (PC) above this particular frequency. Fig. 3b presents the $-Z''(\omega)$ curves in various temperatures, it is noted that $-Z''$ decreases when the frequency increases until to a particular frequency, and afterward $-Z''$ rises with the frequency. Above this particular frequency, we note the presence of an asymmetric crest, which shows the relaxation behavior within $\text{Cs}_2\text{AgSbCl}_6$. The

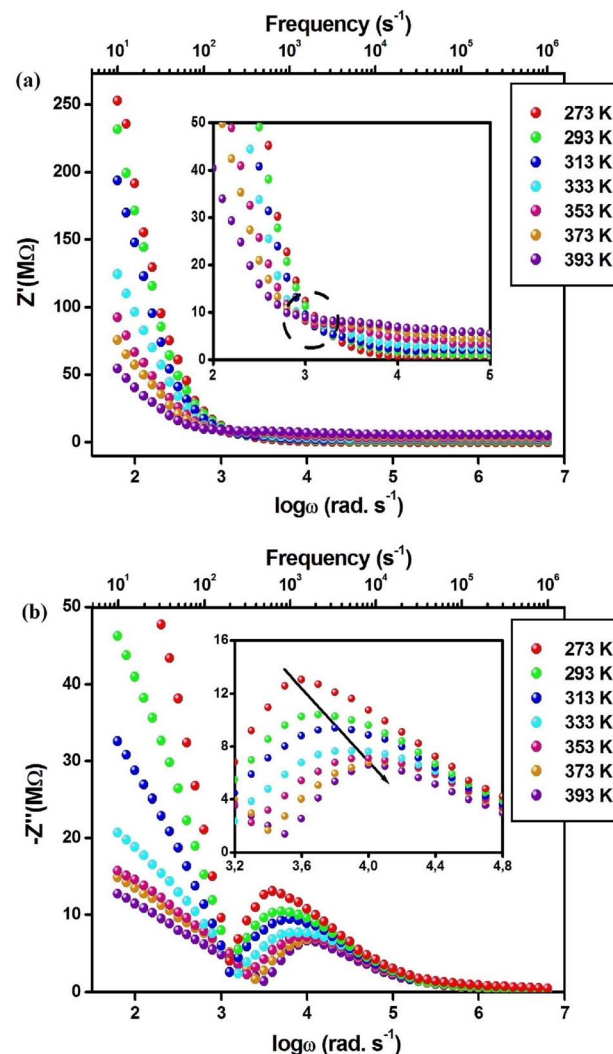


Fig. 3 (a) Real part of impedance (Z') vs. frequency at different temperatures. (b) Imaginary of impedance ($-Z''$) vs. frequency at different temperatures.

improvement of the capacitance is shown by the decrease of $-Z''$ magnitude when the temperature increases.³⁷ Fig. 4a shows the thermal variation of the peak frequency, which increases with the temperature. This behavior confirms that the relaxation process is thermally activated within $\text{Cs}_2\text{AgSbCl}_6$.³⁸ The thermal variation of the relaxation time τ ($\tau = 1/\omega_{\max}$) is shown in Fig. 4a, the order of τ (microseconds) indicates the creation of space charges within $\text{Cs}_2\text{AgSbCl}_6$. Based on the literature, the presence of space charges is related to the redistribution of charge carriers within the crystal structure possesses a relaxation time of around microseconds.³⁸ Fig. 4a shows that τ decreases as temperature increases. This comportment indicates that the charge carriers' delocalization is thermally activated within $\text{Cs}_2\text{AgSbCl}_6$. For high temperatures, this increase in delocalization proposes the passage from non-Debye to Debye-type relaxation.³⁹

$$\tau = \tau_0 \exp\left(-\frac{E_a}{k_B T}\right) \quad (3)$$

Table 2 Composition analysis: chemical elements proportions in $\text{Cs}_2\text{AgSbCl}_6$ SC

Vibrational modes	Raman (cm^{-1})	
	Our experimental study	Other DFT analysis ^{19–21}
$F_{2g}^{(1)}$	73	43.5, 54.4, 28.6
$F_{2g}^{(2)}$	122	110.3, 116.8, 123.4
$E_g^{(1)}$	209	220.2, 194.8, 195.8
A_{1g}	294	290.4, 300.6, 310.6

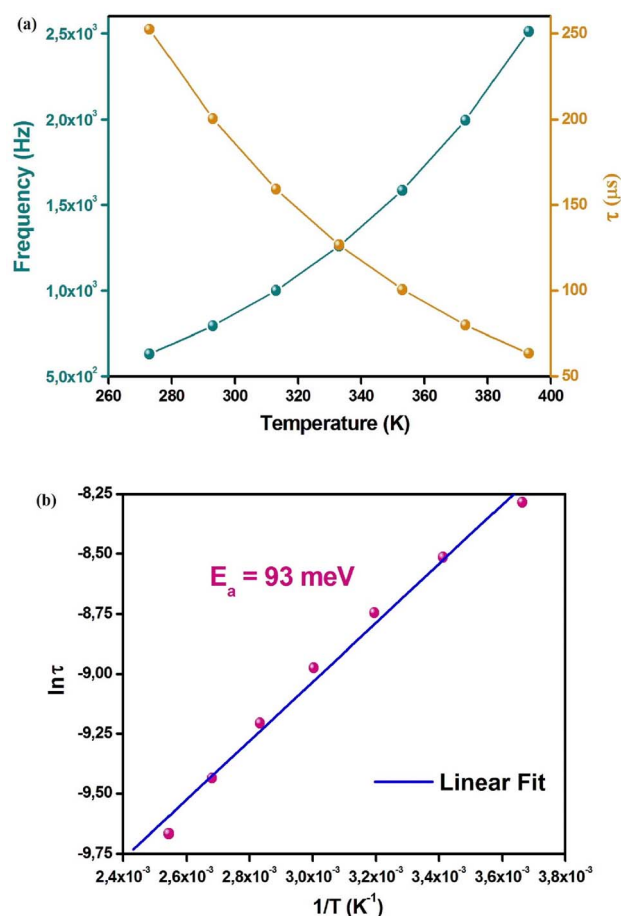


Fig. 4 (a) Temperature dependence of the maximum frequency of $-Z''(\omega)$ and the relaxation time (τ). (b) Arrhenius plot.

where E_a , τ_0 , and k_B present the activation energy, the relaxation time constant, and the Boltzmann constant, respectively.

The fit of the curve (Fig. 4b) was used to calculate the activation energy, which was equal to 93 meV. This typical value of E_a shows the charge carriers' motion within $\text{Cs}_2\text{AgSbCl}_6$. Moreover, this can be assigned to the activation of the polarons motion process with a progressive decrease in electron-lattice coupling.

In order to study the dielectric properties within $\text{Cs}_2\text{AgSbCl}_6$, eqn (4)–(6) have been used to calculate the frequency-dependent complex dielectric permittivity.

$$\varepsilon(\omega) = \varepsilon'(\omega) + j\varepsilon''(\omega) \quad (4)$$

$$\varepsilon'(\omega) = \frac{Z''}{\omega C_0 (Z'^2 + Z''^2)} \quad (5)$$

$$\varepsilon''(\omega) = \frac{Z'}{\omega C_0 (Z'^2 + Z''^2)} \quad (6)$$

$$\tan(\delta) = \varepsilon'(\omega)/\varepsilon''(\omega) \quad (7)$$

where $\varepsilon'(\omega)$ and $\varepsilon''(\omega)$ present the dielectric constant and the dielectric loss, respectively.

Fig. 5a shows the $\varepsilon'(\omega)$ plots at different temperatures, it is noted that in low frequencies, the dielectric constant takes on high values, which can be related to their intrinsic polar character. The entities $[\text{AgCl}_6]^{5-}$ and $[\text{SbCl}_6]^{3-}$ present a polar character since the electronegativity variation between Ag/Sb and Cl (Cl–Ag = 1.23, Cl–Sb = 1.11), the dynamic disorder, which is created by the electronegativity variation among both entities and the bending Cl–Sb–Cl and Cl–Ag–Cl liaisons, fractures the inversion symmetry causing thus the polarization of the $\text{Cs}_2\text{AgSbCl}_6$ lattice. Fig. 5a shows that the dielectric constant decreases as the frequency increases until a particular frequency, then ε' rises with frequency before reaching a constant value at 10^4 Hz. Fig. 5b shows that the transition frequency increases with the temperature. The off-centering character of the Ag and Sb cations can influence the ionic movements within the $[\text{AgCl}_6]^{5-}$ and $[\text{SbCl}_6]^{3-}$ entities, this operation can explain the transition frequency origin. The thermal behavior of the transition frequency can be interpreted by the lattice expansion within $\text{Cs}_2\text{AgSbCl}_6$, since the Ag–Cl, and Sb–Cl distance vary. According to the literature, this off-centering behavior can lead to a ferroelectric nature, but there is no proof of the ferroelectric character within $\text{Cs}_2\text{AgSbCl}_6$.³⁹ The arrows presented in Fig. 5a show a large PC for $d\varepsilon'/dT$ under the transition frequency and then becomes a small NC above this frequency. This transition from PC to NC was noted in some perovskite materials such as $\text{Cs}_{0.06}\text{FA}_{0.79}\text{MA}_{0.15}\text{Pb}(\text{I}_{0.85}\text{Br}_{0.15})_3$ and $\text{CH}_3\text{NH}_3\text{PbI}_3$ at 150 and 10^3 Hz, respectively.^{40,41} According to the literature, the variation in $d\varepsilon'/dT$ behavior can be related to the photo-induced lattice distortion, which causes entropy increment and temperature-dependent variation in the dipole dispersion.³⁹ Fig. 5c shows the thermal variation of ε' at particular frequencies, it is noted the disappearance of relaxation after the frequency 10^4 Hz. This suggests that in the high-frequency region the polar variation becomes lower, and the unrelaxed dielectric constant value shows the electronic and atomic polarization. The dielectric constant behavior can be related to the ionic polarization under the transition frequency. The ionic polarization in $\text{Cs}_2\text{AgSbCl}_6$, which their primitive unit cell contains different ions 6 Cl^- , 2 Cs^+ , Sb^{3+} , and Ag^+ , occurs due to the separation of cations (Cs^+) and anions ($[\text{AgCl}_6]^{5-}$ and $[\text{SbCl}_6]^{3-}$) centers. This type of polarization relates to the deformational element of polarizability. The thermal variation in Sb–Cl, and Ag–Cl chemical bonds will provoke increased ionic polarization when the temperature increases and a large PC for $d\varepsilon'/dT$ appears. The dipolar polarization can explain the dielectric constant behavior after the transition frequency. In illumination, the polarization can be explained by the electrostatic potential gradients, which are created by the inhomogeneous charged distribution. The improved haphazard thermal movement, which drives an important variation from the perfect dielectric alignment, is the reason for increasing dipolar polarization with the temperature. Nevertheless, $d\varepsilon'/dT$ presents low NC since the deviation is slight with the temperature increase. Fig. 5d shows the $\varepsilon''(\omega)$ plots at different temperatures, it is noted that, at low frequencies, the dielectric loss increases



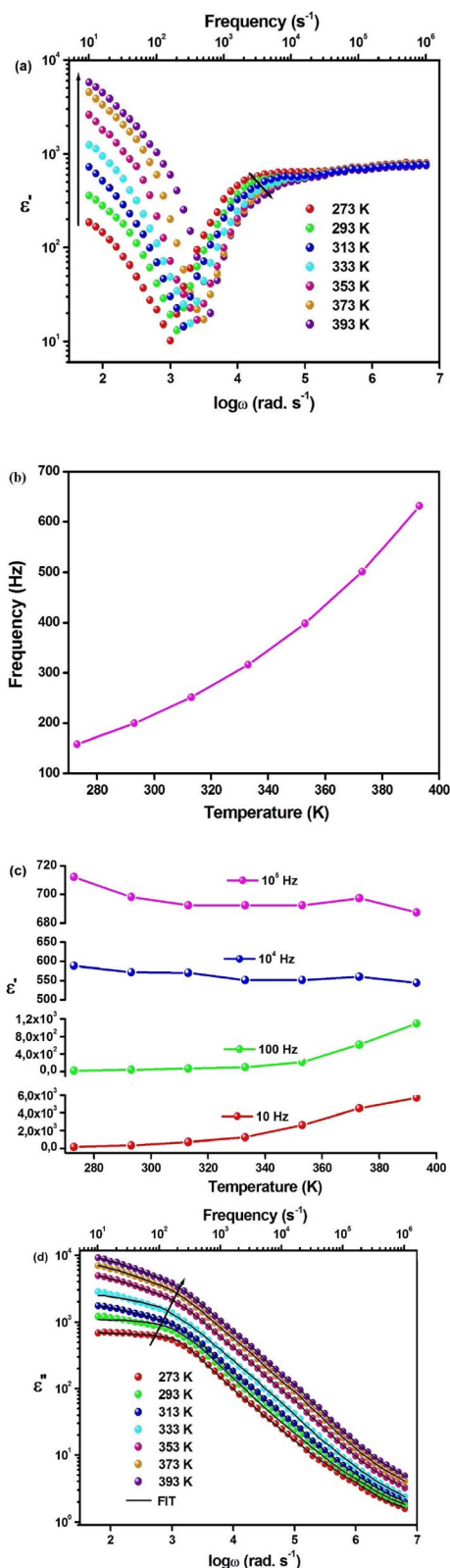


Fig. 5 (a) Variation of $\epsilon'(\omega)$ at different temperatures. (b) Temperature dependence of the transition frequency. (c) Temperature dependence of dielectric constant ϵ' at different frequencies. (d) Variation of $\epsilon''(\omega)$ at different temperatures.

with the temperature. This behavior can be interpreted by the Stevels approach, which proposed that the relaxation procedure appears owing to the vibrational, dipole, and conduction losses.^{42,43}

As reported by the Stevels model, ϵ'' is shown as:

$$\epsilon'' = A\omega^m, (m < 0) \quad (8)$$

$$m = \frac{-4k_B T}{W_{\max}} \quad (9)$$

where A , and, W_{\max} refer to a constant and the maximum barrier height between two traps, respectively.

The parameter m values, which are calculated from the adjusted $\epsilon''(\omega)$ plots (Table 3), increase with the temperature. Consequently, W_{\max} decreases with increasing temperature, which facilitates the motion of charge carriers. The conductivity improvement with the temperature is related to the reduction of the trap's contribution. Moreover, this approach might be applied to the polaron creation since the thermal variation of the parameter m proves the polaron motion in the prepared compound. Herein, the maximum barrier height between the two trap states (W_{\max}) would be indicated as the polaron hopping energy (W_H).³⁹ Under the light, the deformation of the $\text{Cs}_2\text{AgSbCl}_6$ lattice occurs owing to its polar character as we explained lately. A polaron can be a "small polaron" or a "large polaron", this depends on the polaron radius compared to the lattice constant. Within the perovskite $\text{Cs}_2\text{AgSbCl}_6$, a short-term occurs *via* distortion potential and small polarons type, since the structural isolation among the entities $[\text{AgCl}_6]^{5-}$ and $[\text{SbCl}_6]^{3-}$ causes zero-dimensionality (electronic). Within the unit cell, small polarons' motion happens through thermally excited hopping. Fig. 6a shows the polaron creation within the $\text{Cs}_2\text{AgSbCl}_6$ lattice unit under the light. Usually, the conduction activation energy (E_σ) in semiconductors materials is shown as follows:³⁹

$$E_\sigma = W_H + E_s \quad (10)$$

where W_H and E_s represent the hopping energy of the polaron and the energy needed to produce a charge carrier, respectively.

In this work, it was proposed polaronic conduction within $\text{Cs}_2\text{AgSbCl}_6$ so the E_s , which generally presented the semiconductors band gap, describes the transition between E_f (Fermi energy) and E_p (polaronic localized state). According to

Table 3 The calculated ' m ' values from the fitted $\epsilon''(\omega)$ plots at different temperatures

Temperature	Value of ' m '
273	−0.65
293	−0.69
313	−0.73
333	−0.78
353	−0.82
373	−0.87
393	−0.91

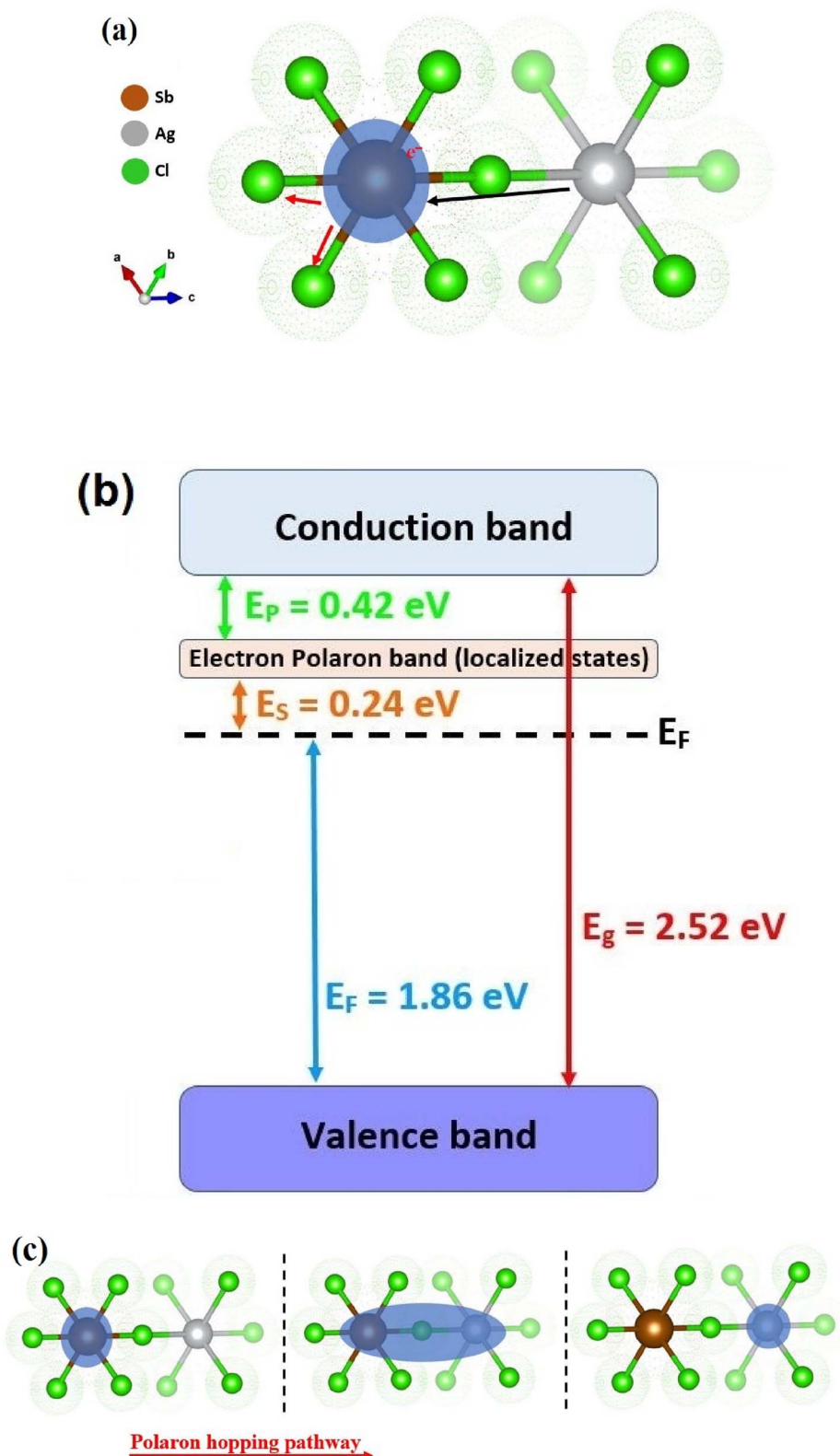


Fig. 6 (a) Polaron creation within the $\text{Cs}_2\text{AgSbCl}_6$ lattice site. Dark and red arrows illustrate repulsive and attractive forces, respectively. (b) Schematic band diagram for $\text{Cs}_2\text{AgSbCl}_6$. (c) Polaron hopping passage in the $\text{Cs}_2\text{AgSbCl}_6$ lattice units.

the literature, the $\text{Cs}_2\text{AgMCl}_6$ ($M = \text{In, Bi, and Sb}$) compounds are assumed to be n-type semiconductors,^{12,44} and the Fermi level of $\text{Cs}_2\text{AgSbCl}_6$ situated above 1.86 eV from the valence

band.¹² The value of W_H , which was determined from eqn (7), is equal to 0.21 eV. Therefore, the value of E_p is 0.42 eV, since $E_p = 2W_H$.^{39,45} Fig. 6b shows the graphic representation of the energy



bands within $\text{Cs}_2\text{AgMCl}_6$. Contrary to free charge carrier motion, polaron hopping is proposed as the suitable conduction mechanism within $\text{Cs}_2\text{AgMCl}_6$, since the room temperature thermal energy is lower than E_p energy. The calculated values of E_s and the appropriate activation energy for conduction can equal 0.24 and 0.43 eV, respectively. The polaron hopping motion from one entity to another one is shown in Fig. 6c. The motion of polarons improves under the temperature effect, and polarons shift different unit cells with the temperature rise.³⁹ Fig. 7 shows the $\tan \delta(\omega)$ plots at different temperatures, it is noted that the loss factor increase with frequency until the transition frequency, and after it the loss factor decrease with the frequency rise. As temperature increases, the shift of the loss tangent's transition frequency towards higher frequencies parallels the observed trend in ϵ' (Fig. 5b). The $d(\tan \delta)/dT$ variation from NC to PC at the transition frequency can be interpreted the same as given for the dielectric loss. Nevertheless, besides the dielectric relaxation, a prospective study will be necessary to clarify this transition and to get an understanding of electric field relaxation.

The electric modulus is shown as follows:⁴⁶

$$M^* = \frac{1}{\epsilon^*} = \frac{1}{(\epsilon' + j\epsilon'')} = \frac{\epsilon'}{\epsilon'^2 + \epsilon''^2} + i \frac{\epsilon''}{\epsilon'^2 + \epsilon''^2} = M' + iM'' \quad (11)$$

where M' and M'' present the real and imaginary parts of the electric modulus, respectively.

Fig. 8a shows the $M'(\omega)$ plots at different temperatures. Under the transition frequency, M' gets a petite value (about zero), and after it M' increases with frequency until reaches an almost constant value after 10^4 Hz. Below the transition frequency (low frequencies), the comportment of $M'(\omega)$ can be explained mainly by the negligence of the electrode polarization.^{47–50} Above the transition frequency, the increase of M' can be interpreted by the polarons hopping.^{47–50} It is noted

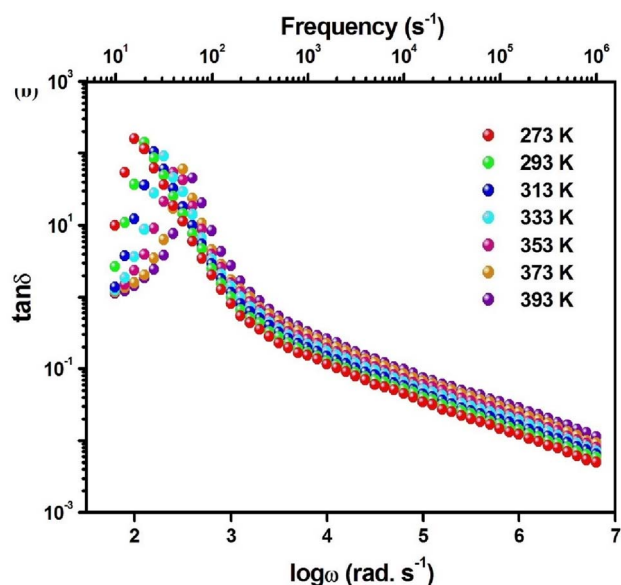


Fig. 7 Variation of $\tan \delta$ at different temperatures.

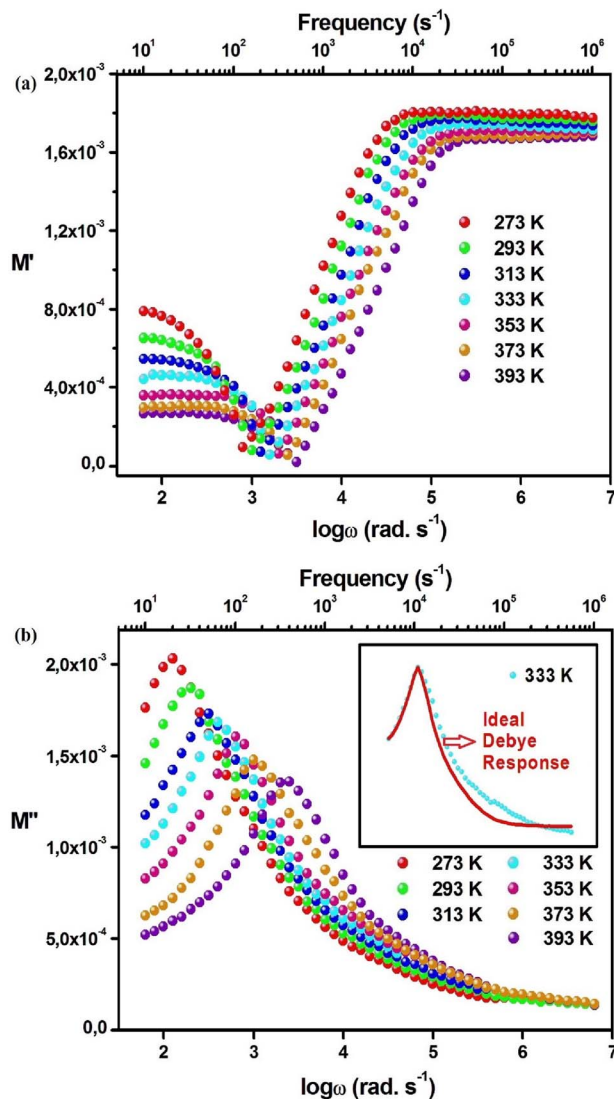


Fig. 8 (a) Variation of $M'(\omega)$ at different temperatures. (b) Variation of $M''(\omega)$ at different temperatures.

that $M'(\omega)$ plots move to a high frequency with the temperature increasing. This behavior shows the temperature impact on the polaron delocalization.^{46–49} Fig. 8b shows the $M''(\omega)$ plots at different temperatures, it is noted the presence of a peak at every temperature. This confirms the existence of electric field relaxation within $\text{Cs}_2\text{AgSbCl}_6$. The asymmetrical nature of $M''(\omega)$ plots show the non-Debye behavior within $\text{Cs}_2\text{AgSbCl}_6$.^{35,37} Nevertheless, this asymmetrical nature shifts to symmetric with the temperature increasing. This behavior proposes a transition in the relaxation process from the non-Debye to the Debye type.³⁹ Fig. 8b shows that the relaxation peak, which presents the transition from long-range to short-range mobility of polarons, shifts to a high frequency with the temperature increasing. This comportment confirms the thermally-activated relaxation process and the long-range mobility amelioration of polarons, which verifies the relaxation passage from the non-Debye to Debye type.^{51–53} Confined polarons can cross the potential barrier with the help of the energy resulting from the

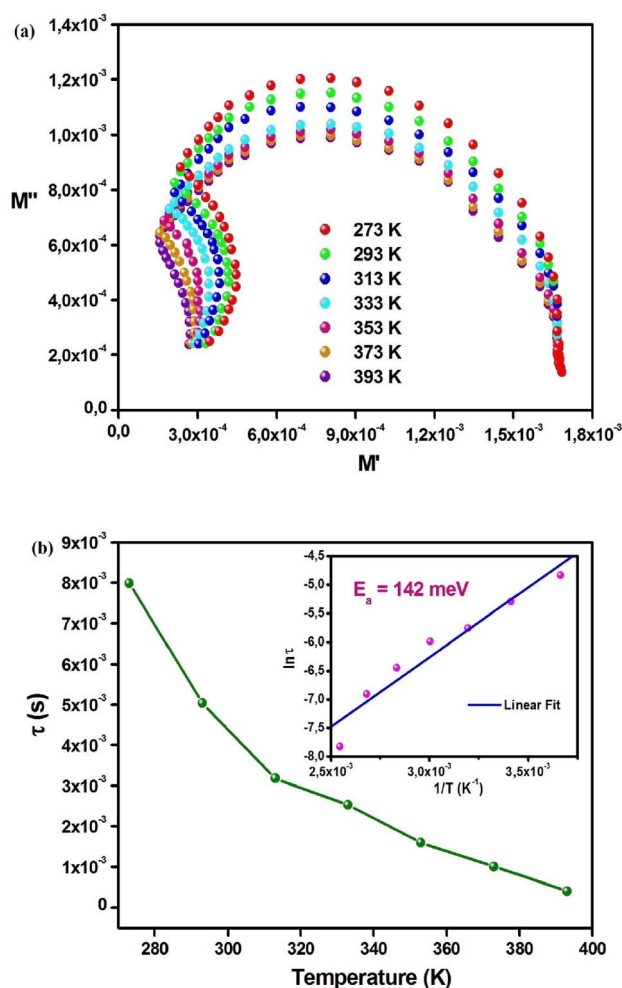


Fig. 9 (a) Modulus Nyquist diagram at different temperatures. (b) Temperature dependence of the relaxation time (τ). The inset presents the Arrhenius plot.

increase in temperature. Fig. 9a, which shows the modulus Nyquist curves at different temperatures, confirms this interpretation by the change of plots from a depressed semicircle to a less depressed semicircle with the rising temperature. Fig. 9b shows the determined relaxation time from $M''(\omega)$ plots at different temperatures. It is noted that τ decreases with increasing temperature, this confirms the thermally activated polaron delocalization within $\text{Cs}_2\text{AgSbCl}_6$.^{54,55} The fit of $\ln(\tau)$ vs. $1/T$ (the inset of Fig. 9a) was used to calculate the activation energy, which was equal to 142 meV.

The charge carriers' motion as well as the relaxation type (non-Debye/localized or Debye/delocalized) can be determined by the association of $M''(\omega)$ and $-Z''(\omega)$ plots. The coincidence of impedance and modulus peaks (M''_{max} and $-Z''_{\text{max}}$) at the same frequency proposes a long-range motion, otherwise, the conduction process explains by a short-range motion. Fig. 10 shows an important mismatching between M''_{max} and $-Z''_{\text{max}}$ peaks at 273 and 393 K. This shift proposed a short-range motion of polarons within $\text{Cs}_2\text{AgSbCl}_6$ and shows the deviation from the ideal Debye response. Fig. 10 shows that when the

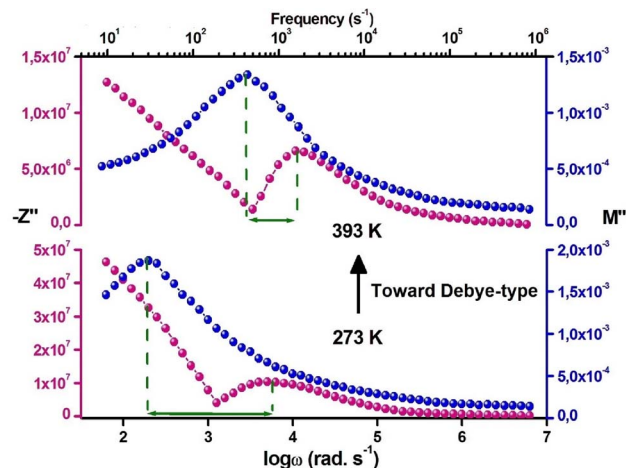


Fig. 10 Correlation of $-Z''(\omega)$ and $M''(\omega)$ plots at 273 and 393 K.

temperature increases the shift between the peaks decreases. Consequently, we deduce that the temperature increase results in the delocalized polarons relaxation (to Debye-type) within $\text{Cs}_2\text{AgSbCl}_6$.^{56,57}

Furthermore, to substantiate the conduction mechanism and delineate the attributes of polarons, transient absorption spectroscopy was conducted through excitation at a 350 nm wavelength. The resultant spectral profile is displayed in Fig. 11a. Within the wavelength range of 450 to 700 nm, we detected a photoinduced absorption (PIA) band, signifying the establishment of self-trapped states (STS) situated below the band edge. This expansive PIA band is a customary observation during the creation of STS, as reported in previous studies.²⁶ The magnitude of the PIA signal registers enhancement up to 850 fs, succeeded by a rapid decline and reduction spanning around 15 ps. The complete progression of photoinduced absorption (PIA) kinetics within the scope of probe wavelengths unfolds within approximately 400–650 fs. The absence of a discernible potential barrier separating free excitons and carriers within self-trapped states (STSs) is evidenced by the swift emergence of PIA kinetics.

A biexponential decay model was used to investigate the kinetics found at 435 nm, which corresponds to the absorbance band edge of the $\text{Cs}_2\text{AgSbCl}_6$ crystal. As shown in Fig. 11b, the results show that the decay may be explained by two separate time constants: τ_1 (1.1 ps, accounting for 77.3% of the decay) and τ_2 (7.4 ps, accounting for 32.7% of the decay). A similar research was also conducted in the 450–650 nm region, with an emphasis on kinetics at 620 nm. As shown in Fig. 10b, this set of kinetics may be described by time constants $\tau_1 = 0.1$ ps and $\tau_2 = 6.3$ ps. The rapid component τ_1 (1.1 ps) discovered in the kinetics at 435 nm can be attributed to carrier relaxation by interaction with longitudinal optical (LO) phonons, known as Fröhlich polarons.^{58,59} Fröhlich polarons develop within lead-halide perovskites, and their creation period is generally approximately 0.1 ps. Notably, this timescale is quite near to the fast time constant reported at 620 nm ($\tau_1 = 0.1$ ps). The resulting deformation of the pliable lattice containing the



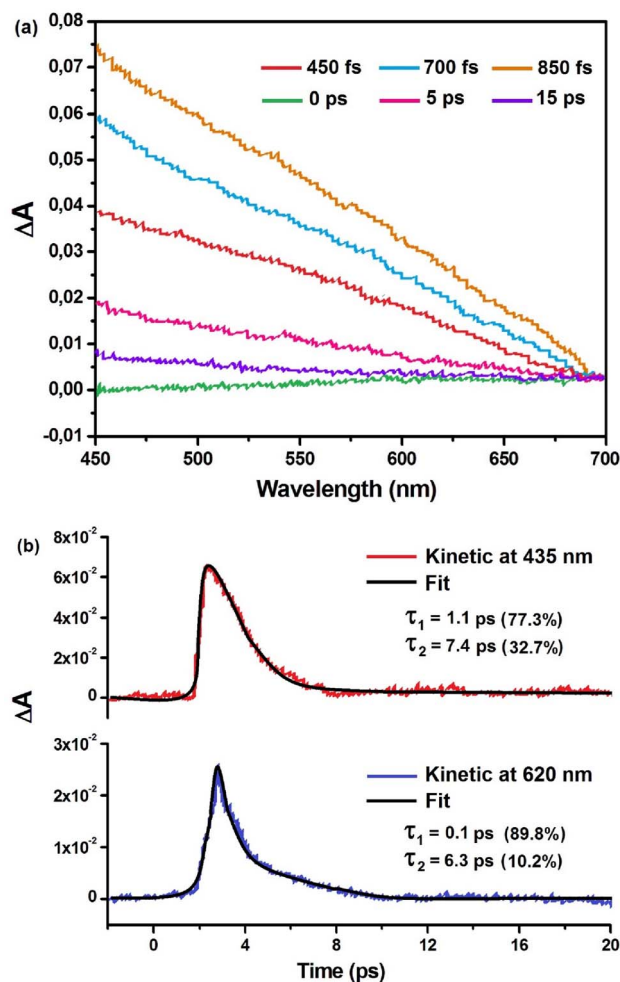


Fig. 11 (a) Transient absorption spectra in femtosecond scale (fs-TA) of $\text{Cs}_2\text{AgSbCl}_6$ SC in the 450–700 nm probe range following 340 nm laser stimulation. (b) Continuous black lines illustrate the exponential fit of the experimental data at 435 and 620 nm.

dimensions of the Fröhlich polaron causes various acoustic phonon modes to be activated. The interaction of electrons with acoustic phonons, together with the fast self-confinement of carriers caused by these acoustic phonons, supports the development of the secondary component seen at 435 and 620 nm. These events are anticipated to occur at $\tau_2 = 7.4$ ps and $\tau_2 = 6.3$ ps, respectively.

4. Conclusions

In sum, the dielectric and conduction process within $\text{Cs}_2\text{-AgSbCl}_6$ have been studied through the EIS as a function of temperature. This work shows that the dielectric constant within $\text{Cs}_2\text{AgSbCl}_6$ falls at a transition frequency, which increases with the temperature. $d\epsilon'/dT$ demonstrates a large PC under the transition frequency and then becomes a small NC above this frequency. Stevels approach, which proves the polaron hopping as a conduction mechanism within $\text{Cs}_2\text{-AgSbCl}_6$, indicates the decreasing of confined charge density when the temperature increases and then conduction improves.

The energy E_p , which is equal to 0.42 eV, is bigger than the ambient-temperature thermal energy, this proposes that the polaron hopping is the principal conduction process within $\text{Cs}_2\text{AgSbCl}_6$. Moreover, the increase in temperature causes the delocalized polarons relaxation (to Debye-type) in $\text{Cs}_2\text{AgSbCl}_6$. The transient absorption kinetics findings point to the implication of small polarons in the capture of carriers within their domains. Once elevated to an excited state, carriers proceed through a relaxation sequence, binding with LO phonons to shape Fröhlich polarons. Subsequently, diverse modes of acoustic phonons come into substantial interaction with charge carriers, culminating in the emergence of small polarons. These small polarons engender self-trapped conditions, effectively constraining charge carriers within a limited number of lattice units. This paper offers the fundamental process behind the dielectric and conduction behaviors within $\text{Cs}_2\text{AgSbCl}_6$.

Conflicts of interest

There are no conflicts to declare.

References

- 1 C. Sun, J. A. Alonso and J. Bian, *Adv. Energy Mater.*, 2020, **11**(2), 2000459.
- 2 C. Yu, *JPhys Energy*, 2019, **1**, 022001.
- 3 M. Usman and Q. Yan, *Crystals*, 2020, **10**(2), 62.
- 4 L. Chouhan, S. Ghimire, Ch. Subrahmanyam, T. Miyasaka and V. Biju, *Chem. Soc. Rev.*, 2020, **49**(10), 2869–2885.
- 5 L. Zhang, Y. Fang, L. Sui, J. Yan, K. Wang, K. Yuan, W. L. Mao and B. Zou, *ACS Energy Lett.*, 2019, **4**(12), 2975–2982.
- 6 C. Sun, J. A. Alonso and J. Bian, *Adv. Energy Mater.*, 2020, **11**(2), 2000459.
- 7 E. F. S. Rodrigues, C. A. Escanhoela, B. Fragoso, G. Sombrio, M. M. Ferrer, M. C. Álvarez-Galván, M. T. Fernández-Díaz, J. A. Souza, F. F. Ferreira, C. Pecharrómán and J. A. Alonso, *Ind. Eng. Chem. Res.*, 2021, **60**(51), 18918–18928.
- 8 A. S. Kshirsagar and A. Nag, *J. Chem. Phys.*, 2019, **151**(16), 161101.
- 9 L. R. Morss, M. P. Siegal, L. Stenger and N. M. Edelstein, *Inorg. Chem.*, 1970, **9**(7), 1771–1775.
- 10 W. Huang, H. Peng, Q. Wei, J. Xia, X. He, K. Bao, Y. Tian and B. S. Zou, *Adv. Opt. Mater.*, 2023, **11**(10), 2203103.
- 11 J. Dahl, W. T. Osowiecki, Y. Cai, J. K. Swabeck, Y. Bekenstein, M. Asta, E. M. Chan and A. P. Alivisatos, *Chem. Mater.*, 2019, **31**(9), 3134–3143.
- 12 J. Dahl, W. T. Osowiecki, Y. Cai, J. K. Swabeck, Y. Bekenstein, M. Asta, E. M. Chan and A. P. Alivisatos, *Chem. Mater.*, 2019, **31**, 3134–3143.
- 13 A. S. Kshirsagar and A. Nag, *J. Chem. Phys.*, 2019, **151**(16), 161101.
- 14 A. H. Slavney, T. Hu, A. M. Lindenberg and H. I. Karunadasa, *J. Am. Chem. Soc.*, 2016, **138**, 2138–2141.
- 15 K. M. McCall, C. C. Stoumpos, S. S. Kostina, M. G. Kanatzidis and B. W. Wessels, *Chem. Mater.*, 2017, **29**(9), 4129–4145.
- 16 J. Pal, S. Manna, A. Mondal, S. Das, K. V. Adarsh and A. Nag, *Angew. Chem., Int. Ed.*, 2017, **56**, 14187–14191.



- 17 S. E. Creutz, E. N. Crites, M. C. De Siena and D. R. Gamelin, *Nano Lett.*, 2018, **18**, 1118–1123.
- 18 Y. Bekenstein, J. Dahl, J. Huang, W. T. Osowiecki, J. K. Swabeck, E. M. Chan, P. Yang and A. P. Alivisatos, *Nano Lett.*, 2018, **18**, 3502–3508.
- 19 H. Lei, D. Hardy and F. Gao, *Adv. Funct. Mater.*, 2021, **31**, 2105898.
- 20 L. Zhou, Y. Xu, B. Chen, D. Kuang and C. Su, *Small*, 2018, **14**(11), 1703762.
- 21 J. Dahl, W. T. Osowiecki, Y. Cai, J. K. Swabeck, Y. Bekenstein, M. Asta, E. M. Chan and A. P. Alivisatos, *Chem. Mater.*, 2019, **31**, 3134–3143.
- 22 B. A. Connor, L. Leppert, M. D. Smith, J. B. Neaton and H. I. Karunadasa, *J. Am. Chem. Soc.*, 2018, **140**, 5235–5240.
- 23 T. T. Tran, J. R. Panella, J. Chamorro, J. R. Morey and T. M. McQueen, *Mater. Horiz.*, 2017, **4**, 688–693.
- 24 J. Zhou, X. Rong, M. S. Molokeev, X. Zhang and Z. Xia, *J. Mater. Chem. A*, 2018, **6**, 2346–2352.
- 25 A. S. Kshirsagar and A. Nag, *J. Chem. Phys.*, 2019, **151**(16), 161101.
- 26 M. B. Bechir and S. Znaidia, Understanding the polaron behavior in CS2CUSBCL6 halide double perovskite, *Phys. Chem. Chem. Phys.*, 2023, **25**, 19684–19692.
- 27 See <http://mill2.chem.ucl.ac.uk/tutorial/lmgp/celref.htm>.
- 28 A. Singh, R. Chaurasiya, A. Bheemaraju, J. Chen and S. Satapathi, *ACS Appl. Energy Mater.*, 2022, **5**, 3926–3932.
- 29 C. Liu, H. Chen, P. Lin, H. Hu, Q. Meng, L. Xu, P. Wang, X. Wu and C. Cui, *J. Mater. Sci.: Mater. Electron.*, 2022, **33**, 24895–24905.
- 30 J. Peng, C. Q. Xia, Y. Xu, R. Li, L. Cui, J. K. Clegg, L. M. Herz, M. B. Johnston and Q. Lin, *Nat. Commun.*, 2021, **12**(1), 1531.
- 31 Y. Guo, Y. Lou, J. Chen and Y. Zhao, *ChemSuschem*, 2021, **15**(3), e202102334.
- 32 G. Volonakis, M. R. Filip, A. A. Haghighirad, N. Sakai, B. Wenger, H. J. Snaith and F. Giustino, *J. Phys. Chem. Lett.*, 2016, **7**, 1254–1259.
- 33 X. Yang, W. Wang, R. Ran, W. Zhou and Z. Shao, *Energy Fuels*, 2020, **34**, 10513–10528.
- 34 A. Singh, R. Chaurasiya, A. Bheemaraju, J. Chen and S. Satapathi, *ACS Appl. Energy Mater.*, 2022, **5**, 3926–3932.
- 35 M. B. Bechir and M. H. Dhaou, *RSC Adv.*, 2021, **11**, 21767–21780.
- 36 M. B. Bechir, A. Almeshal and M. H. Dhaou, *Mater. Res. Bull.*, 2023, **157**, 112012.
- 37 M. B. Bechir and M. H. Dhaou, *Mater. Res. Bull.*, 2021, **144**, 111473.
- 38 M. B. Bechir, A. Almeshal and M. H. Dhaou, *Ionics*, 2022, **28**, 5361–5376.
- 39 N. K. Tailor, N. Parikh, P. Yadav and S. Satapathi, *J. Phys. Chem. C*, 2022, **126**, 10199–10208.
- 40 N. F. Hoque, M. Yang, Z. Li, N. Islam, X. Pan, K. Zhu and Z. Fan, *ACS Energy Lett.*, 2016, **1**, 142–149.
- 41 M. Jahandar, N. Khan, M. Jahankhan, C. E. Song, H. K. Lee, S. K. Lee, W. S. Shin, M. K. Lee, S. H. Im and S. J. Moon, *J. Ind. Eng. Chem.*, 2019, **80**, 265–272.
- 42 N. K. Tailor and S. Satapathi, *J. Phys. Chem. C*, 2021, **125**, 5243–5250.
- 43 P. Maji, A. Ray, P. Sadhukhan, S. Chatterjee and S. Das, *J. Appl. Phys.*, 2018, **124**(12), 124102.
- 44 W. Deng, Z.-Y. Deng, J. He, M. Wang, Z. Chen, S. Wei and H. Feng, *Appl. Phys. Lett.*, 2017, **111**(15), 151602.
- 45 J. Lago, P. D. Battle, M. J. Rosseinsky, A. I. Coldea and J. Singleton, *J. Condens. Matter Phys.*, 2003, **15**, 6817–6833.
- 46 M. B. Bechir, K. Karoui, M. Tabellout, K. Guidara and A. B. Rhaïem, *Phase Transit.*, 2015, **91**, 901–917.
- 47 P. Sengupta and R. Ray, *Mater. Lett.*, 2021, **302**, 130456.
- 48 M. S. Sheikh, A. P. Sakhya, P. Sadhukhan, A. Dutta, S. Das and T. P. Sinha, *Ferroelectrics*, 2017, **514**, 146–157.
- 49 M. Kumari and P. M. Sarun, *J. Mater. Sci.: Mater. Electron.*, 2021, **33**, 8607–8615.
- 50 S. A. Fatima, R. Shaheen and K. Shahzad, *Appl. Phys. A*, 2021, **127**(6), 466.
- 51 P. Pal and A. Ghosh, *J. Appl. Phys.*, 2021, **129**(23), 234102.
- 52 A. S. Priya, D. Geetha and I. B. S. Banu, *Braz. J. Phys.*, 2021, **51**, 1438–1447.
- 53 F. Ambrosio, D. Meggiolaro, E. Mosconi and F. De Angelis, *ACS Energy Lett.*, 2019, **4**, 2013–2020.
- 54 Z. Raddaoui, S. E. Kossi, R. Brahem, A. Bajahzar, A. V. Trukhanov, A. L. Kozlovskiy, M. V. Zdorovets, J. Dhahri and H. Belmabrouk, *J. Mater. Sci.: Mater. Electron.*, 2021, **32**, 16113–16125.
- 55 M. Selmi, B. Smida and S. E. Kossi, *J. Mater. Sci.: Mater. Electron.*, 2021, **32**, 6014–6027.
- 56 A. O. Çağırtekin, A. Ajjaq, Ö. Barin and S. Acar, *Phys. Scr.*, 2021, **96**, 115807.
- 57 K. Yadagiri and R. Nithya, *J. Phys. Chem. Solids*, 2021, **158**, 110232.
- 58 A. D. Wright, L. R. V. Buizza, K. J. Savill, G. Longo, H. J. Snaith, M. B. Johnston and L. M. Herz, *J. Phys. Chem. Lett.*, 2021, **12**, 3352–3360.
- 59 B. Wu, W. Ning, Q. Xu, M. Manjappa, M. Feng, S. Ye, J. Fu, S. Lie, T. Yin, F. Wang, T. W. Goh, P. C. Harikesh, Y. K. E. Tay, Z. Shen, F. Huang, R. Singh, G. Zhou, F. Gao and T. C. Sum, *Sci. Adv.*, 2021, **7**(8), eabd3160.

